J Adv Ceram

Research Article

Machine-learning-guided discovery of $Ca_3SnSi_2O_9$-based ceramics with ultrahigh *Q×f* values for topological metasurface filters

Kang Du[1,2,✉], Yunkang Ge[1], Beibei Wang[1], Yuan Wang[1], Chengyun Li[1], Anping Lv[1], Yan Liu[1,2], Ying Yang[1,2], Weijia Han[1,2], Guochao Wei[1,2,✉], Wen Lei[3,4], Shengxiang Wang[1,2,✉]

Cite this article: Du K, Ge Y, Wang B, et al. *J Adv Ceram* 2026, **15**(5): 9221285. https://doi.org/10.26599/JAC.2026.9221285

ABSTRACT: Microwave dielectric ceramics have emerged as highly promising materials for high-frequency applications due to their exceptional dielectric properties. Nevertheless, achieving an optimal balance among the interdependent parameters of relative permittivity (ε_r), quality factor (*Q×f*), and temperature coefficient of resonant frequency (τ_f) to satisfy the technical requirements of microwave components continues to pose a substantial challenge. In this work, an interpretable machine learning framework was proposed to elucidate the structure–property relationships, thereby guiding the compositional design of the candidate microwave ceramic $Ca_3SnSi_2O_9$. Based on the machine learning insights, we developed a $Ca_3Sn_{1-x}Ge_xSi_2O_9$ ($0.025 \le x \le 0.20$) ceramic system where controlled Ge^{4+} substitution for Sn^{4+} was strategically designed to synergistically optimize both *Q×f* and τ_f values while maintaining low ε_r. This improvement was achieved through the enhanced relative covalency (r_c) of Sn–O and Si–O bonds, along with intensified octahedral distortion (δ) and polyhedral chain angles (σ) in the single-phase $Ca_3Sn_{1-x}Ge_xSi_2O_9$ ceramics. Remarkably, the $Ca_3Sn_{1-x}Ge_xSi_2O_9$ (x = 0.05) ceramics demonstrated outstanding performance, exhibiting an ultrahigh *Q×f* value of 120,413 GHz coupled with a favorably small negative τ_f value of −25.8 ppm/°C. These results clearly demonstrate that the collaborative optimization strategy can significantly enhance the microwave dielectric properties of $Ca_3SnSi_2O_9$-based ceramics. Furthermore, a single-mode topological metasurface filter operating in the X-band was designed and fabricated using the ultralow dielectric loss $Ca_3Sn_{1-x}Ge_xSi_2O_9$ (x = 0.05) ceramics. Leveraging the bulk-edge correspondence, we established a relationship between structural morphology with transitional deformations and operating frequency. Experimental results demonstrated that the topological metasurface filter can operate at any frequency within the range of 9.6–10.3 GHz. This advancement extends the potential applications of $Ca_3SnSi_2O_9$-based ceramics to metasurface filters for high-frequency communication systems.

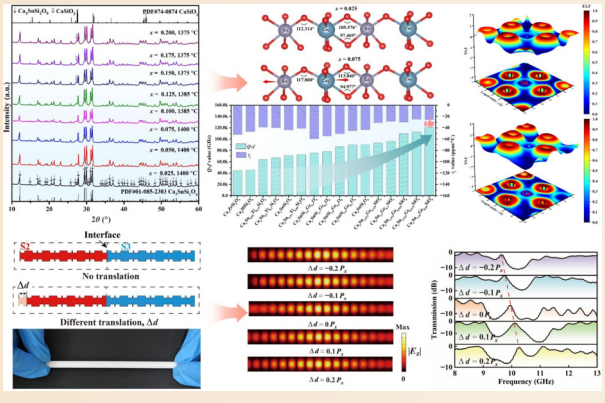

KEYWORDS: $Ca_3SnSi_2O_9$-based ceramics; crystal structural optimization; ultrahigh quality factor (*Q×f*) values; machine learning; topological metasurface filters

1 Introduction

The rapid advancement of millimeter-wave communication and Internet of Things (IoTs) technologies has driven substantial progress in radio frequency components, including dielectric resonators, filters, substrate materials, antenna systems, and capacitive elements [1–5]. In particular, microwave dielectric ceramics have emerged as a critical material system in recent years, offering exceptional benefits in miniaturization, weight reduction, and integrated filter design [6,7]. Among these, low-relative permittivity (ε_r) microwave dielectric ceramic filters stand out due to their superior performance, combining high-speed

[1]School of Microelectronics, Wuhan Textile University, Wuhan 430200, China. [2]Hubei Provincial Engineering Research Center for Wide-Bandgap Semiconductor Materials and Devices, Wuhan Textile University, Wuhan 430200, China. [3]School of Optical and Electronic Information, Key Lab of Functional Materials for Electronic Information (B) of MOE, Huazhong University of Science and Technology, Wuhan 430074, China. [4]Advanced Manufacturing Institute of Huazhong University of Science and Technology in Wenzhou, Zhejiang Key Laboratory of Electronic Functional Ceramics and Devices, Wenzhou 325035, China.

✉ Corresponding authors. E-mail: K. Du, dk@wtu.edu.cn; G. Wei, gcwei@wtu.edu.cn; S. Wang, shxwang@wtu.edu.cn

Received: December 23, 2025; Revised: March 18, 2026; Accepted: March 19, 2026

signal transmission, rapid response times, outstanding signal integrity, low insertion loss, and sharp frequency selectivity. Notably, in one-dimensional topological metasurfaces, the bulk-edge correspondence enables the formation of cavity modes at interfaces between topologically distinct structures [8], supporting phenomena such as rainbow trapping [9], nonreciprocal transmission [10], nonlinear light generation [11], and angle-insensitive transmission [12]. These modes are employed for wave filtering, with the quality factor ($Q\times f$) and bandwidth determined by the unit cells and nontrivial interface domains [13]. Furthermore, introducing an additional parameter dimension allows tuning of the operating frequency within the photonic bandgap [14]. Since electromagnetic waves propagate within dielectric media, the performance of metasurface filters is ultimately governed by the microwave dielectric properties of the substrate material [15]. Therefore, it is advantageous to explore high-performance ceramic substrates with ultralow dielectric loss and high thermal stability.

At millimeter-wave frequencies, three dielectric parameters become paramount: (i) low ε_r to minimize parasitic effects, (ii) high $Q\times f$ values to suppress dielectric losses, and (iii) near-zero resonant frequency (τ_f) values to ensure thermal stability [16,17]. These requirements are particularly stringent for high-frequency filters, where dielectric ceramics must exhibit either ultrahigh $Q\times f$ values exceeding 100,000 GHz or ultralow dielectric loss equivalents [18–20]. Low ε_r and ultrahigh $Q\times f$ values are primarily observed in aluminate [21–26], silicate [27–31], and germanate [32–38] ceramics owing to their predominantly tetrahedral crystal structures. This behavior arises from the strong covalent character of their primary chemical bonds (Al–O, Si–O, and Ge–O) [39,40]. However, the application of some ultrahigh $Q\times f$ and low-ε_r microwave dielectric ceramics is limited by several factors, including high raw material costs [24,32–38], the presence of volatile and variable-valence elements, moisture absorption tendencies, and large negative τ_f values [21–23,27,29]. Notably, $Ca_3MSi_2O_9$ (M = Sn, Zr, and Hf) ceramics, which exhibit a cuspidine-type crystal structure featuring an interconnected framework of [MO_6] octahedra and [CaO_7] decahedral chains and [SiO_4] double tetrahedra, are free from volatile or variable-valence elements [41]. These ceramics also demonstrate excellent high-temperature stability among silicates. Furthermore, high $Q\times f$ values (90,500 GHz) and a small negative τ_f (−43.3 ppm/℃) were obtained in the low-ε_r $Ca_3SnSi_2O_9$ ceramics [42], indicating that ultrahigh $Q\times f$ (≥ 100,000 GHz) and near-zero τ_f values may be achieved through further optimization of the crystal structure in the $Ca_3SnSi_2O_9$ ceramics.

In our previous work, the $Q\times f$ and τ_f values of $Ca_3SnSi_2O_9$-based ceramics were related to the relative covalency (r_c) of Sn–O and Si–O bonds and polyhedral distortion, respectively [41,42]. Furthermore, an increase in the r_c of Sn–O and Si–O bonds contributed to improving $Q\times f$ values, and increased polyhedral distortion within the crystal framework enhanced the restoring force of the central cation in the polyhedron, thereby controlling the τ_f values to be closer to zero [43]. The order r_c (Ge–O) > r_c (Si–O) > r_c (Sn–O) > r_c (Al–O) was observed in microwave dielectric ceramics [18,40], and the Ge^{4+} cation also exhibited sixfold coordination with O^{2-} anions, forming a regular octahedron [33]. Notably, in contrast to previous studies where Ge^{4+} substitution for smaller Si^{4+} only marginally increased r_c (Si/Ge–O) in $Ca_3SnSi_2O_9$-based ceramics [42], the designed substitution of Ge^{4+} for larger Sn^{4+} is expected to significantly enhance r_c (Sn–O) and intensify octahedral distortion (δ). This synergistic effect may concurrently optimize both the $Q\times f$ and τ_f values of the $Ca_3SnSi_2O_9$-based ceramics.

Furthermore, the inverse design of materials using artificial intelligence (AI) to regulate composition and properties has been extensively explored [44]. By developing suitable machine learning models, researchers can uncover the intrinsic mechanisms governing $Q\times f$ values [45], thereby informing the optimization pathways for ceramics. Inspired by machine learning-derived strategies for enhancing the $Q\times f$ value of $Ca_3SnSi_2O_9$-based ceramics, this work investigates the substitution of Sn^{4+} with the smaller Ge^{4+} cation. To this end, we systematically replaced Sn^{4+} (coordinate number (CN) = 6) with Ge^{4+} (CN = 6) [46] in $Ca_3Sn_{1-x}Ge_xSi_2O_9$ ($0.025 \le x \le 0.20$) ceramics, which were synthesized via a solid-state reaction. The phase composition, micromorphology, and microwave dielectric properties were thoroughly characterized to determine the substitution limit and identify the factors responsible for achieving ultrahigh $Q\times f$ and minimal $|\tau_f|$ values in single-phase materials. Based on these insights, a cooperative optimization strategy for $Q\times f$ and τ_f was proposed and validated. Furthermore, the practical potential of these high-$Q\times f$ ceramics was demonstrated by designing, fabricating, and testing a topological metasurface filter for X-band applications.

2 Experimental

2.1 Matching of the machine learning model

The primary workflow for predicting the $Q\times f$ value of $Ca_3SnSi_2O_9$-based ceramics using interpretable machine learning methods in this study is illustrated in Fig. S1 in the Electronic Supplementary Material (ESM). The $Q\times f$ value is influenced not only by material compositions but also by process conditions and dielectric properties, all of which are equally important and cannot be overlooked. To accurately predict the $Q\times f$ value, we first prepared 57 high-quality and densified ceramics (with densification above 95%) under stringent process control. This ensured the comparability of all data within this small sample dataset. Next, nine features from three key aspects were extracted, including the material composition, process system, and dielectric properties. A detailed description of these features is provided in Table S1 in the ESM. Then, a comprehensive dataset and feature set were constructed. The dataset was further divided into training, validation, and test subsets at a 6 : 3 : 1 ratio. To further enhance the small-sized dataset while maintaining a consistent sample distribution (Fig. S2 in the ESM), sample augmentation technique was applied to enhance the subsets except the test subset [47,48]. Subsequently, various feature selection methods were compared to eliminate redundant features, and extensive performance matching was conducted across different machine learning models, including the generalized additive model (GAM), least squares boosting (LSBoost), extreme gradient boosting (XGBoost), backpropagation neural network (BPNN), and an ensemble model (MLP-RF) combining a multilayer perceptron (MLP) and random forest (RF). Finally, optimized matching performance was achieved using the Northern Goshawk Optimization (NGO) intelligent algorithm, which is evaluated by the root mean square error (RMSE) and coefficient of determination (R^2).

Under the premise of achieving the optimal matching effect, shapley additive explanations (SHAP) and partial dependence plot (PDP) interpretability techniques were employed to analyze the model's decision-making process. These techniques help determine the trend of how different features impact the $Q\times f$ value and identify the specific ranges of feature values required by the model to achieve a high $Q\times f$ value. They accelerate the design of material compositions by providing actionable insights into the key factors influencing the model's output.

2.2 Synthesis and property analysis of $Ca_3SnSi_2O_9$-based ceramics

The $Ca_3Sn_{1-x}Ge_xSi_2O_9$ ($0.025 \le x \le 0.20$) ceramics were synthesized via a conventional solid-state reaction method. High-purity powders of $CaCO_3$ (99.9%, Sinopharm), SnO_2 (99.9%, 50–70 nm, Aladdin), SiO_2 (99.9%, Sinopharm), and GeO_2 (99.9%, Aladdin) were used as starting materials. All raw materials were weighed according to the stoichiometric formula of $Ca_3Sn_{1-x}Ge_xSi_2O_9$ ($0.025 \le x \le 0.20$) and mixed with zirconia balls in deionized water for 5 h. The resulting slurry was dried at 100 °C for 24 h, and the obtained powders were then calcined at 1300 °C for 5 h to yield pre-sintered powders. These calcined powders were further ball-milled for 5 h and dried to obtain fine materials. The resultant powders were mixed with 8% polyvinyl alcohol (PVA) and then compacted into cylinders. Finally, the specimens were sintered at 1375–1400 °C for 5 h to obtain dense ceramics.

The phase purity of the samples was examined using an X-ray diffractometer (XRD; X'Pert PRO, PANalytical, the Netherlands), and Rietveld refinement was performed using FullProf software to extract crystal structural parameters. High-resolution transmission electron microscopy (HRTEM) and selected-area electron diffraction (SAED) were conducted on a transmission electron microscope (Tecnai G2 F30, FEI, USA). The microstructure of the sintered specimens was characterized using a field-emission scanning electron microscope (FE-SEM; Gemini SEM 300, Zeiss, Japan). Room-temperature infrared reflectivity spectra were acquired using a Fourier transform-infrared spectrometer (FT-IR; IFS 66v, Bruker, Germany) at the beamline station of the National Synchrotron Radiation Laboratory (NSRL, China). The microwave dielectric properties and performance of the metasurface filters were measured using a network analyzer (Keysight E5063A, Keysight, USA) [49]. The ε_r versus temperature under various frequencies was determined using an impedance analyzer (4294A, Agilent, USA) and a VDMS-2000 system (Partulab, China).

2.3 First-principles calculations of $Ca_3SnSi_2O_9$-based ceramics

The density functional theory (DFT) computations conducted in this study were accomplished using the Vienna *Ab initio* Simulation Package (VASP) [50,51]. The computational parameters were set as follows: Exchange-correlation interactions were characterized within the framework of the generalized gradient approximation (GGA) by applying the Perdew–Burke–Ernzerhof (PBE) functional [52,53]. A plane-wave basis set with a kinetic energy cutoff value of 520 eV was adopted, and Brillouin zone (BZ) integration for static self-consistent field (SCF) calculations was executed with a Γ-centered $2 \times 4 \times 4$ k-point mesh. The convergence criteria for electronic iterations and ionic relaxations were designated as 1×10^{-6} eV and −0.02 eV/Å, respectively. The topological analysis of the electron localization function (ELF) [54] was implemented using the Multiwfn code [55,56], which possesses powerful abilities in processing wavefunction-derived properties.

3 Results and discussion

3.1 Design of $Ca_3SnSi_2O_9$-based ceramics via interpretable machine learning model

The matching performance of the machine learning models was investigated and is presented in Fig. 1 and Figs. S3–S5 in the ESM. As shown in Fig. 1(a1), feature selection methods such as the Kendall, Spearman, maximal information coefficient, Pearson, and relief methods rely solely on univariate statistics to rigidly eliminate features. This approach fails to capture the multicollinearity behind $Q\times f$ and tends to mistakenly remove weakly correlated features with synergistic effects, leading to unstable statistical estimation and loss of key physical mechanisms. In contrast, L2 regularization employs coefficient shrinkage rather than feature elimination, automatically

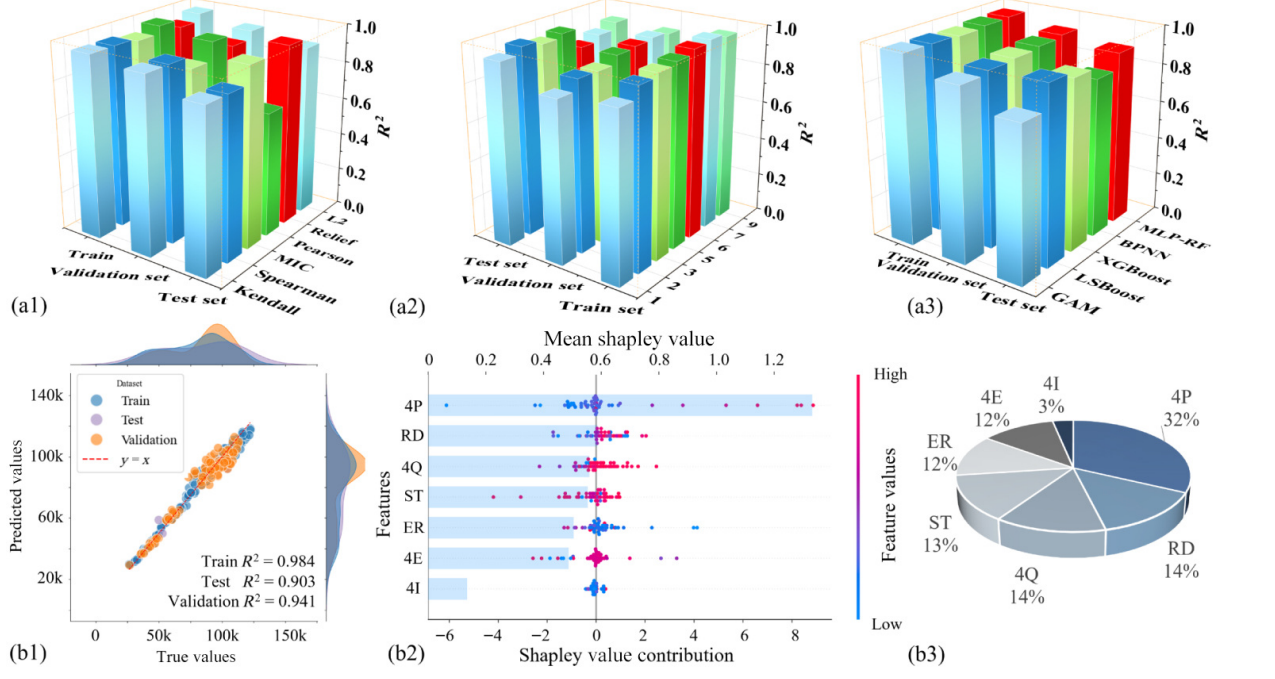

Fig. 1 Matching performance of machine learning models: Comparisons of (a1) different feature selection methods, (a2) different numbers of features, and (a3) different models. (b1) Detailed comparisons of R^2 values in subsets, (b2) feature importance reflected by mean Shapley value and SHAP swarm plot, and (b3) feature contributions.

distributing weights among collinear features while retaining all features. It stabilizes parameter estimation under small-sample conditions and allows the model to utilize the conditional contributions of weakly correlated features, thereby more accurately characterizing the multifactor synergistic response mechanism of $Q\times f$ and achieving superior predictive performance. In Fig. 1(a2), when the number of features is less than 3, the R^2 on the validation set is relatively low, remaining below 0.9. The model achieves the best overall R^2 value when the number of features reaches 7. As demonstrated in Fig. 1(a3), the MLP-RF model exhibits the highest R^2 values with minimal variability across subsets, while the other single models show poorer performance on the test set or greater variability among subsets. In the prediction of $Q\times f$ for $Ca_3SnSi_2O_9$-based ceramics, single models such as GAM, LSBoost, XGBoost, and BPNN fail, whereas the MLP-RF ensemble model succeeds. The fundamental reason lies in the inability of the former to simultaneously address the three core challenges of this task: the overfitting risk due to high-dimensional small-sample data, feature competition caused by strong multicollinearity, and the difficulty in capturing complex nonlinear mechanisms and synergistic effects. Specifically, GAM lacks adaptability to unknown nonlinearities due to its predefined functional forms. Although LSBoost and XGBoost can handle nonlinear relationships, the greedy splitting behavior of tree models in small-sample settings tends to mistake noise for signals and inadequately captures fine-grained feature interactions. BPNN, constrained by its shallow architecture, struggles to learn deep representations and is sensitive to initialization, often converging to local optima. In comparison, the MLP-RF ensemble model projects raw features into a more robust latent space through the deep nonlinear transformations of the MLP, effectively decoupling collinearity and extracting high-order interactive features. It then leverages RF's ensemble bagging mechanism to provide stable estimation and noise filtering for small-sample data. This complementary architecture combines deep representation learning with ensemble decision optimization, preserving the MLP's ability to fit complex physical mechanisms while utilizing the RF's randomness to escape the MLP's local optima traps. Ultimately, it achieves accurate modeling of the multifactor synergistic response mechanism of $Q\times f$. The matching performance of the MLP-RF model is shown in Fig. 1(b1), where Fig. S6 in the ESM presents the performances in each subset. With appropriate regularization and training strategies, overfitting could be effectively mitigated. In this model, both the R^2 values of the subsets and the differences in errors between subsets were optimized comprehensively, indicating strong generalization capability. As a result, the MLP-RF model was selected for this study.

To gain a comprehensive understanding of the model's decision-making process and to elucidate the specific impacts of features on the $Q\times f$ value, the SHAP interpretability technique was employed. Specifically, the SHAP summary plot illustrates the importance of each feature, while the SHAP heatmap reflects the distribution of SHAP values for different features across all samples in the dataset. Initially, based on the summary plot and contributions in Figs. 1(b2) and 1(b3), the features 4P, relative density (RD), and 4Q were the three most influential features affecting the $Q\times f$ value. Their respective importance proportions were 32%, 14%, and 14%, accounting for a total contribution of 60%. The SHAP values for the 4P feature exhibited a broad distribution, ranging from −6 to 8, indicating significant variability in the distribution of these features within the dataset. Additionally, a higher 4P feature value is beneficial for improving the predicted $Q\times f$ value.

In Fig. 2(a), the distributions of feature values across all samples were identified. For instance, the 4P feature has high SHAP values from a sample size of approximately 50, indicating that it has the most significant and positive impact on the $Q\times f$ value among these samples. To investigate the impact trends and tipping points of various features on the $Q\times f$ value, the GAM model was used to fit the one-dimensional SHAP scatter plot of the features, as shown in Fig. 2(b). Taking the 4P feature as an example, the SHAP scatter change trend of the 4P feature can be well captured by the model, with an R^2 of 0.8355 and a significance p value below 0.05, indicating that this change trend can explain the influence trend of 4P feature values on the predicted $Q\times f$ value. To visualize the influence patterns of individual features on the model outputs, multiple trend-fitting methods were systematically compared. Based on this evaluation, a high-complexity GAM model with parameters nsplines = 50 and $\lambda = 0.001$ was ultimately selected as the standard tool for analyzing the 4P features. This configuration offers sufficient flexibility to capture complex nonlinear relationships while maintaining favorable smoothing properties, thereby enabling clear and interpretable visualization of feature influence patterns. It was found that a tipping point exists at a 4P value of 1.52, beyond which the impact of the 4P feature on the $Q\times f$ value shifts from positive to negative. Specifically, the 4P feature refers to the dielectric polarizability of tetravalent cations (Ge^{4+}, Sn^{4+}, and Si^{4+}) in $Ca_3Sn_{1-x}Ge_xSi_2O_9$ ceramics, which reflects their ability to distort the surrounding electron cloud under an external electric field. As a key parameter associated with dielectric polarization, 4P directly influences ionic

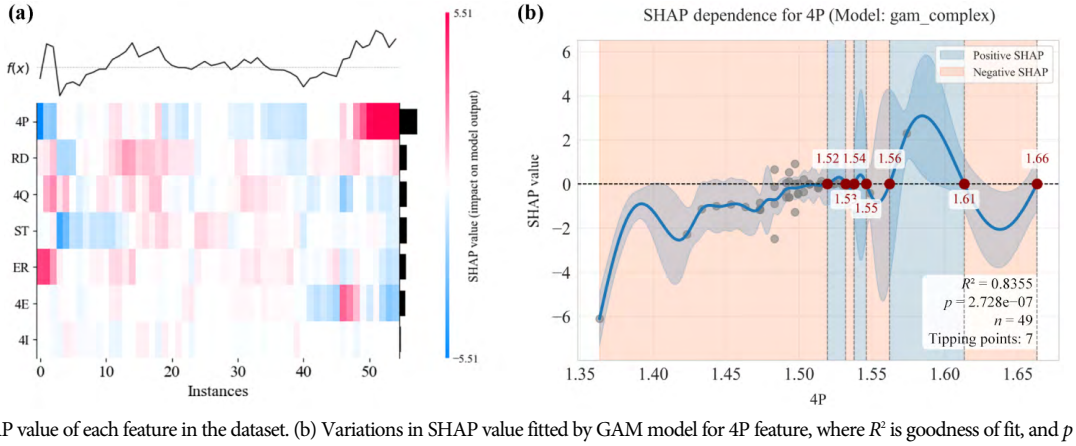

Fig. 2 (a) SHAP value of each feature in the dataset. (b) Variations in SHAP value fitted by GAM model for 4P feature, where R^2 is goodness of fit, and p value indicates significance level.

and electronic polarization within the crystal structure. A moderate increase in 4P enhances the polarization response while preserving structural stability, thereby improving the $Q\times f$ value by reducing polarization relaxation loss. However, when 4P exceeds the tipping point of 1.52, excessive polarizability induces severe electron cloud distortion in the [Sn/GeO_6] and [SiO_4] polyhedra. This distortion intensifies lattice vibrations and increases intrinsic dielectric loss, which explains the transition of the impact of the 4P feature on $Q\times f$.

The significance of interaction effects between features was assessed through p value tests derived from analysis of variance, with the aim of highlighting both the strength and directional influence of these interactions on the prediction of $Q\times f$ values. To account for multiple comparisons, the p values were adjusted using the Bonferroni correction. The resulting p value matrix is provided in Fig. S7 in the ESM. The majority of interaction effects had p values exceeding 0.05, suggesting insufficient evidence for significant interaction effects between feature pairs under the present statistical and data conditions. Given these results, PDP was employed to further elucidate the synergistic influence of features on the $Q\times f$ value, as depicted in Figs. 3(a1)–3(b3). Figure 3 shows the synergistic effect of 4P features and other features on the $Q\times f$ value. Taking the 4P and RD feature pair as an example, when the 4P feature value is higher than 1.7 and the RD value is higher than 0.978, the model tends to lower the prediction of the $Q\times f$ value. When the 4P feature value is lower than 1.55, and the RD value is higher than 0.982, the model tends to provide higher $Q\times f$ prediction values. Excessive 4P (> 1.7) causes severe lattice distortion even in dense ceramics (RD > 0.978), increasing intrinsic dielectric loss. In contrast, moderate 4P (< 1.55) combined with high density (RD > 0.982) minimizes both polarization relaxation and pore-induced dielectric losses, favoring higher $Q\times f$ values. The impact of other features can be determined by referring to this analysis.

3.2 Phase compositions, microstructure, and crystal structural analysis of $Ca_3Sn_{1-x}Ge_xSi_2O_9$ ($0.025 \le x \le 0.20$)

Based on the interpretable analysis of the machine learning (ML) model, it is possible to clearly determine the impact trend and transition interval of each feature on the $Q\times f$ value and identify the approximate range of material components and process details that are beneficial to the $Q\times f$ value. Based on the value range of feature parameters, our proposed ML model provides numerous material system choices; however, for $Ca_3Sn_{1-x}Ge_xSi_2O_9$ ceramics, the first four most important feature values all fall within the range that is conducive to improving the $Q\times f$ value. Thus, an ultrahigh $Q\times f$ value of 115,740 GHz can be predicted. Guided by the machine learning prediction scheme, we used smaller Ge^{4+} ions to substitute larger Sn^{4+} ions and successfully synthesized a series of $Ca_3Sn_{1-x}Ge_xSi_2O_9$ ceramics. The XRD patterns of the $Ca_3Sn_{1-x}Ge_xSi_2O_9$ ($0.025 \le x \le 0.20$) ceramics, sintered at their optimal temperatures, were initially analyzed to investigate the solubility limit of Ge^{4+} substitution for Sn^{4+}. As illustrated in Fig. 4(a), the substitution of Ge^{4+} reduced the densification temperature of the $Ca_3Sn_{1-x}Ge_xSi_2O_9$ ($0.025 \le x \le 0.20$) ceramics. Single-phase compositions were observed in $Ca_3Sn_{1-x}Ge_xSi_2O_9$ ($0.025 \le x \le 0.125$) ceramics, while further Ge^{4+} substitution ($0.15 \le x \le 0.20$) led to the formation of a minor $CaSiO_3$ second phase in $Ca_3Sn_{1-x}Ge_xSi_2O_9$ ($0.15 \le x \le 0.20$) ceramics. Rietveld refinement was performed to determine the detailed phase compositions and crystal structural parameters of the $Ca_3Sn_{1-x}Ge_xSi_2O_9$ ($0.025 \le x \le 0.20$) ceramics. The refinement results (Fig. 4(b), Fig. S8 and Table S2 in the ESM) demonstrated excellent agreement between the measured and fitted XRD patterns, supported by low refinement error factors, confirming the reliability of the refinement. The $Ca_3Sn_{1-x}Ge_xSi_2O_9$ ($0.025 \le x \le 0.125$) ceramics exhibited a monoclinic structure ($P2_1/c$ space group), corresponding with the standard card (JCPDS No. 01-085-2303). However, for compositions with $0.15 \le x \le 0.20$, a $CaSiO_3$ second phase (5.73–7.64 wt%) was detected, suggesting that the maximum Ge^{4+} solubility in $Ca_3Sn_{1-x}Ge_xSi_2O_9$ ceramics likely occurred at x = 0.125. Notably, Ge^{4+} could also substitute for Si^{4+} in $Ca_3SnSi_2O_9$ ceramics [42]. Therefore, it is essential to confirm whether Ge^{4+} replaces Sn^{4+} or Si^{4+} in $Ca_3Sn_{1-x}Ge_xSi_2O_9$ ceramics.

To examine the effects of Ge^{4+} substitution for Sn^{4+} on the crystal structure, first-principles calculations were performed. The

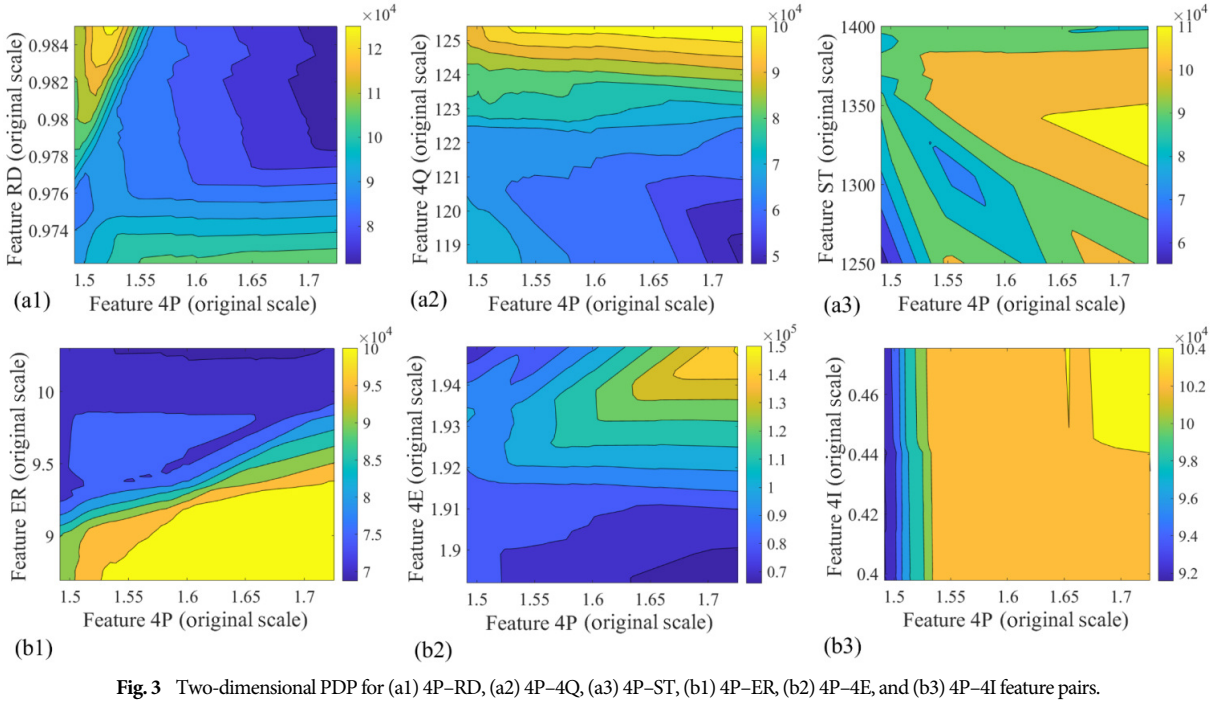

Fig. 3 Two-dimensional PDP for (a1) 4P–RD, (a2) 4P–4Q, (a3) 4P–ST, (b1) 4P–ER, (b2) 4P–4E, and (b3) 4P–4I feature pairs.

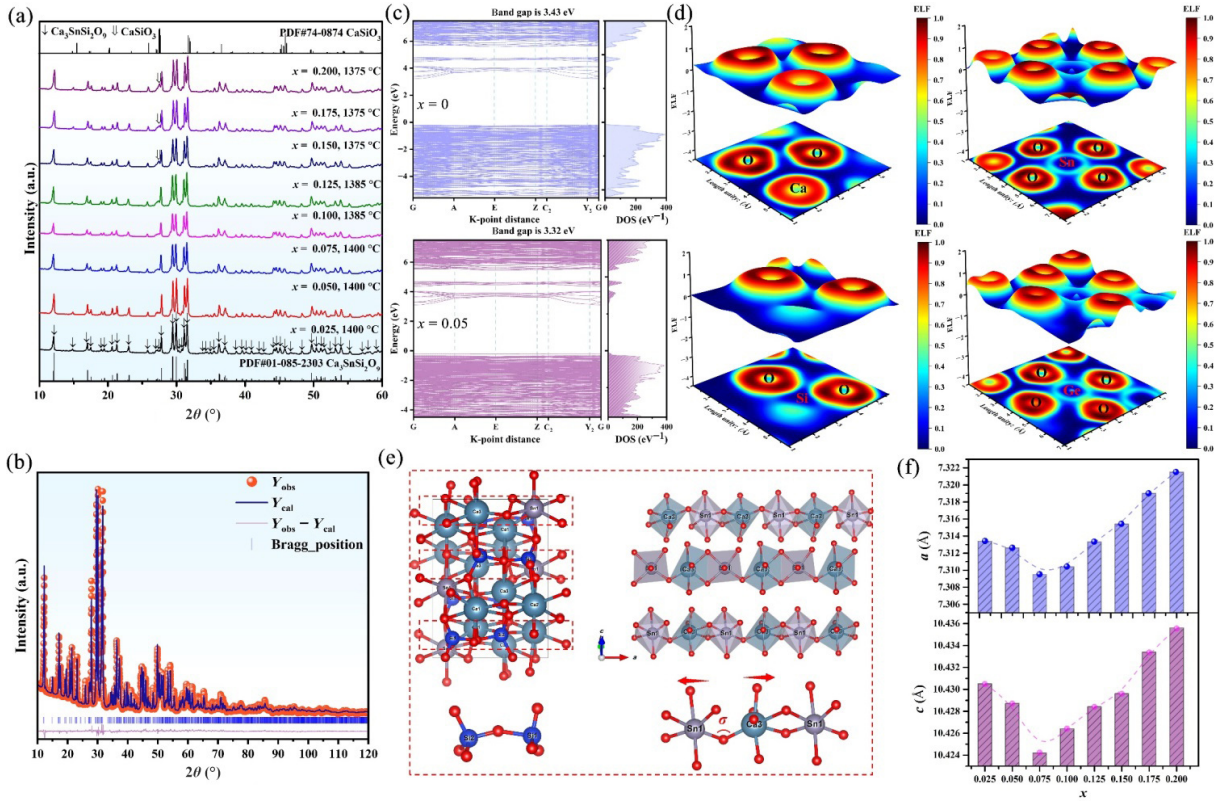

Fig. 4 (a) XRD patterns of $Ca_3Sn_{1-x}Ge_xSi_2O_9$ ($0.025 \le x \le 0.20$) ceramics sintered at their optimal temperatures. (b) Rietveld refinement plot of $Ca_3Sn_{1-x}Ge_xSi_2O_9$ (x = 0.05) ceramics. (c) Energy band structure and E_g of $Ca_3Sn_{1-x}Ge_xSi_2O_9$ (x = 0 and 0.05) ceramics. (d) ELF of $Ca_3Sn_{1-x}Ge_xSi_2O_9$ (x = 0.05) ceramics, (e) crystal structure of $Ca_3SnSi_2O_9$, and (f) evolution of lattice parameters (a and c) as a function of x.

crystal structure was further relaxed to achieve the lowest energy state for $Ca_3Sn_{1-x}Ge_xSi_2O_9$ ceramics. As depicted in Figs. 4(c) and 4(d), the energy band structure, total density of states (DOS), and ELF were calculated. The band structures of $Ca_3Sn_{1-x}Ge_xSi_2O_9$ (x = 0 and 0.05) exhibited similar features, with the band gap (E_g) decreasing gradually from 3.43 (x = 0) to 3.32 eV (x = 0.05) as Ge^{4+} substitution increased. The conduction band minimum remained at the G-point, indicating their insulating behavior. Furthermore, ELF analysis revealed key bonding characteristics [57], where higher ELF values corresponded to greater electron localization [58]. Figure 4(d) displays the ELF distributions for the [CaO_7] decahedron, [SnO_6] octahedron, [SiO_4] tetrahedron, and [GeO_4] tetrahedron in $Ca_3Sn_{1-x}Ge_xSi_2O_9$ (x = 0.05). The ELF values between Ca and O atoms (0.1–0.2) confirmed the ionicity of the Ca–O bond. In contrast, higher ELF values (0.3–0.4) were observed for Si–O and Sn–O bonds, indicating stronger covalent character. Notably, the Ge–O bond exhibited even higher ELF values (0.4–0.5), demonstrating significantly greater covalency than both Si–O and Sn–O bonds. These results suggest that Ge^{4+} substitution enhances the r_c of the Sn–O bond.

The ionic radius of Ge^{4+} (r^{4+}_{Ge} = 0.53 Å, CN = 6; r^{4+}_{Ge} = 0.39 Å, CN = 4) was smaller than that of Sn^{4+} (r^{4+}_{Sn} = 0.69 Å, CN = 6) but larger than that of Si^{4+} (r^{4+}_{Si} = 0.26 Å, CN = 4). Consequently, the substitution of Ge^{4+} for Sn^{4+} was expected to reduce the lattice parameters of $Ca_3Sn_{1-x}Ge_xSi_2O_9$ ceramics. As illustrated in Fig. 4(e), the crystal structure of $Ca_3SnSi_2O_9$ consisted of [CaO_7] decahedra, [SnO_6] octahedra, and [SiO_4] tetrahedra. The framework was built from edge-sharing [CaO_7] decahedra and [SnO_6] octahedra, with the elongated direction aligned along the a-axis. The [SnO_6] octahedra were centrally located within the ribbons, alternating with [CaO_7] decahedra along the a-axis. There is a polyhedral chain angle (σ) between the [SnO_6] octahedra and [CaO_7] decahedra, which can characterize the degree of distortion in the CaO_7–SnO_6 chain. Due to the smaller size of Ge^{4+} compared to Sn^{4+}, its substitution must compress the CaO_7–SnO_6 chains, leading to a contraction in the a-axis lattice parameter. As summarized in Table S2 in the ESM and Fig. 4(f), increasing Ge^{4+} substitution for Sn^{4+} initially caused the lattice parameters (a and c) and unit cell volume (V) to decrease, reaching a minimum value at x = 0.075. This confirmed that low Ge^{4+} content substitution effectively reduced the lattice parameters. However, further Ge^{4+} substitution led to an unexpected expansion. This is attributed to Ge^{4+} no longer occupying the [SnO_6] octahedral sites but instead replacing Si^{4+} in tetrahedral coordination, as the octahedral sites have limited Ge^{4+} solubility. At higher substitution levels ($0.10 \le x \le 0.20$), this shift in substitution preference results in lattice expansion and the eventual precipitation of a second $CaSiO_3$ phase.

Transmission electron microscopy (TEM) and energy dispersive spectroscopy (EDS) analyses were performed to further verify the formation of the $Ca_3Sn_{1-x}Ge_xSi_2O_9$ (x = 0.05) solid solution. As shown in Fig. 5(b), EDS analysis confirmed the homogeneous distribution of Ca, Sn, Ge, Si, and O in the $Ca_3Sn_{1-x}Ge_xSi_2O_9$ (x = 0.05) grains, with no elemental segregation detected. Furthermore, the sharp diffraction spots in the SAED pattern (Fig. 5(c)) align perfectly with the monoclinic structure ($P2_1/c$ space group) along the [$2\bar{2}1$] zone axis, a finding further supported by standard diffraction simulations of $Ca_3Sn_{0.95}Ge_{0.05}Si_2O_9$ (Fig. 5(d)). In addition, HRTEM images along the [$2\bar{2}1$] zone axis (Fig. 5(e)) revealed an interplanar spacing of 5.87 Å for the (110) plane, consistent with the refinement results. The corresponding fast Fourier transform (FFT) patterns exhibited diffraction spots matching both the experimental and simulated SAED patterns. Notably, the inverse fast Fourier transform (IFFT) analysis (inset in Fig. 5(e)) clearly revealed lattice distortions. The potential energy of "lattice distortion" in high-

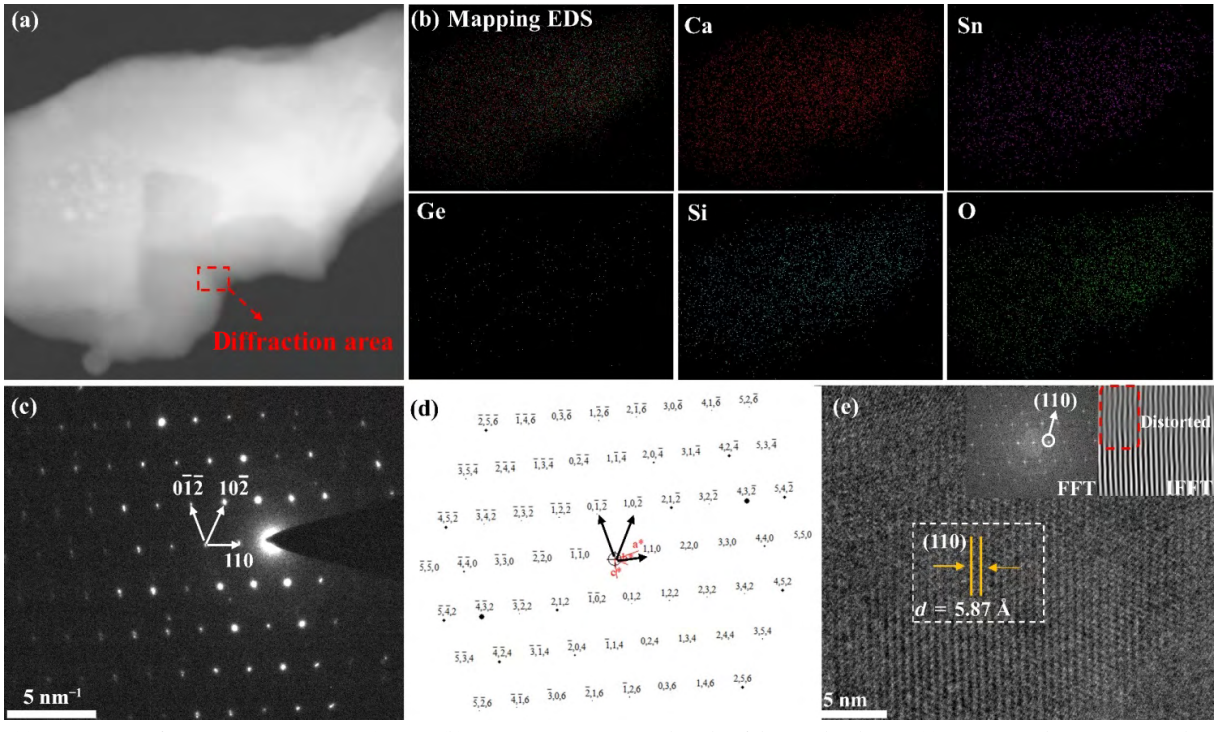

Fig. 5 (a) Grain images of $Ca_3Sn_{1-x}Ge_xSi_2O_9$ ($x = 0.05$) grains. (b) Mapping EDS images and results of element distribution. (c) Experimental SAED patterns along [$2\bar{2}1$] zone axis. (d) Simulated SAED patterns along [$2\bar{2}1$] zone axis. (e) HRTEM, FFT, and IFFT images along [$2\bar{2}1$] zone axis.

entropy ceramics is lower than that of an "ideal lattice", and the elastic distortion energy due to the mismatch of atomic radii and moduli between constituent atoms is further released in the crystal through a change in cell shape [59]. Consequently, the observed lattice distortions in $Ca_3Sn_{0.95}Ge_{0.05}Si_2O_9$ primarily stem from Ge^{4+} substitution at Sn^{4+} sites, given the smaller ionic radius of Ge^{4+}. This contrasts with our earlier work on the $BaMg_2Al_6Si_{9-x}Ge_xO_{30}$ ($x = 0.5$) ceramics, where minor Ge^{4+} substitution at Si^{4+} sites did not induce significant lattice distortion [60]. The IFFT results indicated that a small amount of Ge^{4+} preferentially occupied Sn^{4+} sites in the $Ca_3Sn_{1-x}Ge_xSi_2O_9$ ceramics.

Figure 6 presents the polished and thermally etched surface microstructures of $Ca_3Sn_{1-x}Ge_xSi_2O_9$ ($0.025 \le x \le 0.20$) ceramics. All of the ceramics exhibited dense microstructures characterized by well-defined grains and minimal porosity, with uniform grain distribution. The average grain sizes of the $Ca_3Sn_{1-x}Ge_xSi_2O_9$ solid solutions progressively decreased from 1.0 ($x = 0.025$) to 0.6 μm ($x = 0.15$), demonstrating the significant grain refinement effect of Ge^{4+} substitution in $Ca_3SnSi_2O_9$-based ceramics. No second phases were detected in compositions with $x \le 0.15$. In addition, the $Ca_3Sn_{1-x}Ge_xSi_2O_9$ ($x = 0.20$) ceramics revealed a distinct bimodal microstructure consisting of two grain types, with second phase grains exhibiting diffuse boundaries. To explore the elemental distribution of both grains in the $Ca_3Sn_{1-x}Ge_xSi_2O_9$ ($x = 0.20$) ceramics, EDS analysis (Fig. 6(g)) showed negligible Sn and Ge content in the second phase grains, confirming their identity as the $CaSiO_3$ phase. These microstructural and phase composition characteristics are expected to influence the microwave dielectric properties.

3.3 Microwave dielectric properties and topological metasurface filter applications of the $Ca_3Sn_{1-x}Ge_xSi_2O_9$ ($0.025 \le x \le 0.20$) ceramics

Figure 7 presents the relative density (ρ_{rel}) and microwave dielectric properties of $Ca_3Sn_{1-x}Ge_xSi_2O_9$ ($0.025 \le x \le 0.20$) ceramics sintered at their optimal temperatures. As illustrated in Fig. 7(a), all compositions exhibited high relative densities (> 96%). Notably, single-phase ceramics ($0.025 \le x \le 0.125$) demonstrated higher ρ_{rel} values than undoped $Ca_3SnSi_2O_9$ ceramics [42], suggesting that Ge^{4+} substitution enhanced densification. The observed decrease in ρ_{rel} for multiphase ceramics ($0.15 \le x \le 0.20$) can be attributed to the presence of the low-density $CaSiO_3$ second phase [17]. The experimental relative permittivity ($\varepsilon_{r\text{-}exp}$) decreased monotonically from 8.91 ($x = 0.025$) to 8.51 ($x = 0.20$) with increasing Ge^{4+} content. Since all samples maintained high relative densities (> 96%), the porosity effects on $\varepsilon_{r\text{-}exp}$ were negligible. To elucidate the structure–property relationships, we employed the Phillips–van Vechten–Levine (P–V–L) theory, Clausius–Mossotti (C–M) equations, and bond valence theory. P–V–L-derived susceptibility (χ) calculations (Table S3 in the ESM) revealed that Si–O bonds contributed over 44% (Fig. 7(a) and Fig. S9 in the ESM) of the total susceptibility ($\Sigma\chi$) in all compositions. The nearly constant $\Sigma\chi$ across the series (Table S3 in the ESM) indicates minimal influence of Ge^{4+} substitution on the overall polarizability, implying that the $\varepsilon_{r\text{-}exp}$ reduction cannot be explained by χ changes alone in $Ca_3Sn_{1-x}Ge_xSi_2O_9$ ($0.025 \le x \le 0.20$) ceramics.

At microwave frequencies, ionic displacement polarization dominates the dielectric response, as electronic polarization becomes negligible. Complementary to the P–V–L analysis, the C–M equations predicted a gradual decrease in the calculated relative permittivity ($\varepsilon_{r\text{-}cal}$) from 8.02 to 7.66 with increasing x, mirroring the experimental trend. Furthermore, the corrected relative permittivity ($\varepsilon_{r\text{-}corr}$) of $Ca_3Sn_{1-x}Ge_xSi_2O_9$ ($0.025 \le x \le 0.20$) ceramics was higher than both $\varepsilon_{r\text{-}exp}$ and $\varepsilon_{r\text{-}cal}$ after excluding the influence of porosity. With the increase in x, both $\varepsilon_{r\text{-}exp}$ and $\varepsilon_{r\text{-}corr}$ decreased gradually and showed similar variation trends. The slight systematic deviation between the $\varepsilon_{r\text{-}corr}$ and $\varepsilon_{r\text{-}cal}$ values originated from the "rattling effect" induced by the bond valence

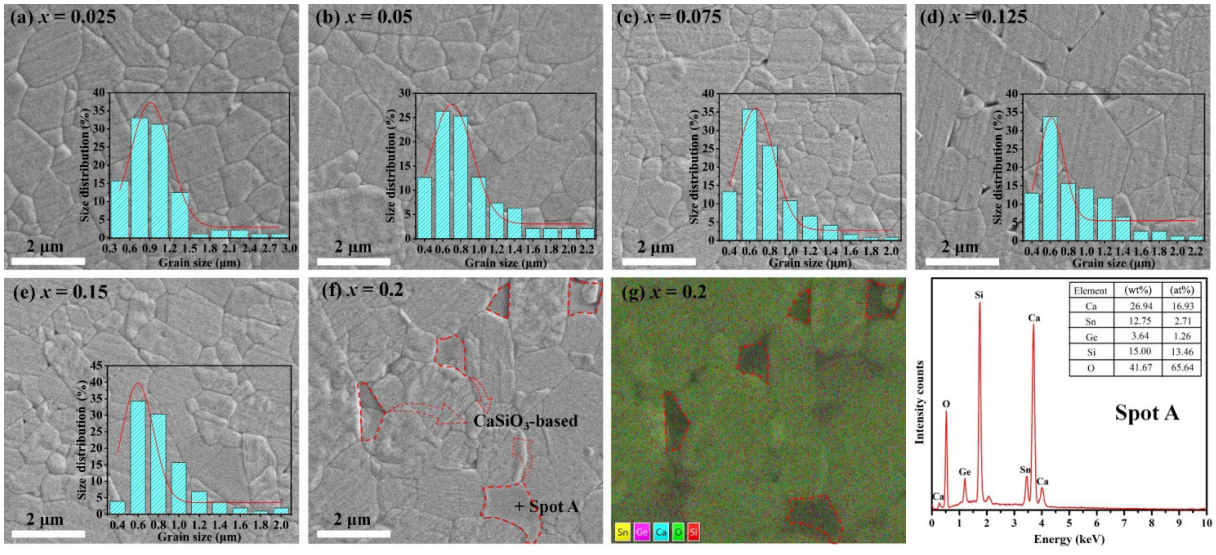

Fig. 6 (a–f) SEM images of thermally etched $Ca_3Sn_{1-x}Ge_xSi_2O_9$ ($0.025 \le x \le 0.20$) ceramics. (g) EDS results of thermally etched $Ca_3Sn_{1-x}Ge_xSi_2O_9$ ($x = 0.20$) ceramics.

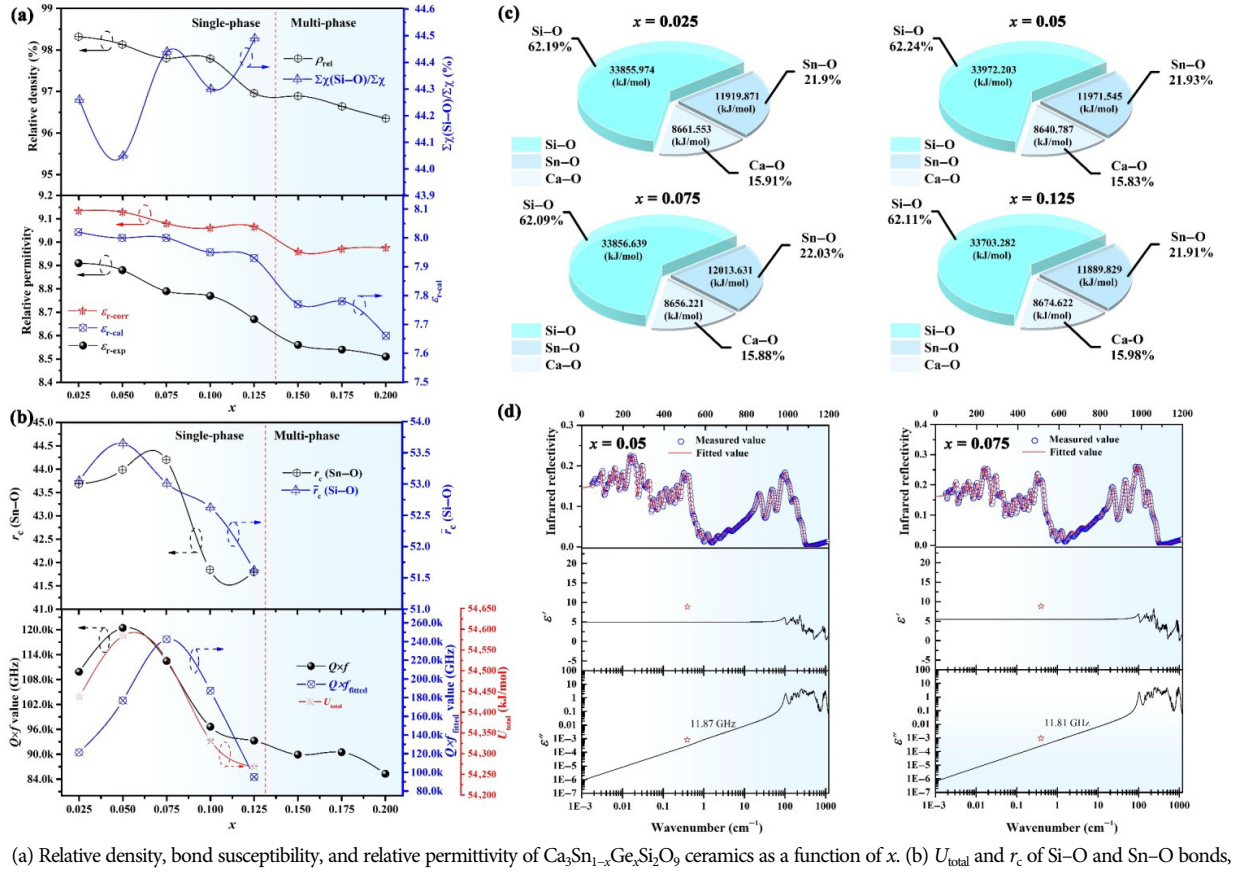

Fig. 7 (a) Relative density, bond susceptibility, and relative permittivity of $Ca_3Sn_{1-x}Ge_xSi_2O_9$ ceramics as a function of x. (b) U_{total} and r_c of Si–O and Sn–O bonds, and $Q \times f$ values of $Ca_3Sn_{1-x}Ge_xSi_2O_9$ ceramics as a function of x. (c) Ratio of $\sum U$(Ca–O), $\sum U$(Sn–O), and $\sum U$(Si–O) to the total lattice energy of $Ca_3Sn_{1-x}Ge_xSi_2O_9$ ceramics. (d) Experimental and fitted far-infrared reflection spectroscopy (IR) of $Ca_3Sn_{1-x}Ge_xSi_2O_9$ ceramics.

deficiency of Sn^{4+} ions (Table S4 in the ESM), which enhanced ionic polarization and consequently increased $\varepsilon_{r\text{-}exp}$ and $\varepsilon_{r\text{-}corr}$. In summary, the $\varepsilon_{r\text{-}exp}$ of single-phase $Ca_3Sn_{1-x}Ge_xSi_2O_9$ ($0.025 \le x \le 0.125$) ceramics was mainly governed by total ionic polarization, while that of multiphase ceramics ($0.15 \le x \le 0.20$) was primarily influenced by phase composition.

As illustrated in Fig. 7(b), the $Q \times f$ values of the $Ca_3Sn_{1-x}Ge_xSi_2O_9$ ceramics initially increased and then decreased with increasing Ge^{4+} substitution. An ultrahigh $Q \times f$ value of 120,413 GHz was achieved in the $Ca_3Sn_{1-x}Ge_xSi_2O_9$ ($x = 0.05$) ceramics, representing an approximately 30% enhancement compared to the undoped $Ca_3SnSi_2O_9$ ceramics [42]. Notably, the $Q \times f$ values exhibited a strong dependence on crystal structural parameters. Based on bond valence theory (ESM), the r_c of chemical bonds could be calculated in Table S4 in the ESM and Fig. 7(b). The Ca–O bond exhibited the lowest average relative covalency ($\overline{r_c}$), with the bond covalency following the trend: $\overline{r_c}$ (Si–O) > r_c (Sn–O) > $\overline{r_c}$ (Ca–O). Unlike Ge^{4+} substitution for Si^{4+}

in $Ca_3SnSi_{2-x}Ge_xO_9$ ceramics [42], which failed to simultaneously optimize $\overline{r_c}$ (Si–O) and r_c (Sn–O), the substitution of smaller Ge^{4+} for Sn^{4+} in $Ca_3Sn_{1-x}Ge_xSi_2O_9$ significantly enhanced both parameters. The maximum r_c for Si–O and Sn–O bonds was achieved at x = 0.05 and x = 0.075, respectively, directly contributing to the improved $Q\times f$ values. As shown in Figs. S10–S12 and Table S5 in the ESM, X-ray photoelectron spectroscopy (XPS) analysis was performed to investigate the element valence states of $Ca_3Sn_{1-x}Ge_xSi_2O_9$ ceramics, and the binding energies of each element (Ca, Sn, Ge, Si, and O) after peak fitting for different Ge^{4+} substitution contents ($0.025 \le x \le 0.125$) are summarized. With the substitution of Ge^{4+} for Sn^{4+}, the binding energy of lattice oxygen gradually increased, while the content of oxygen vacancies was relatively low and showed no significant change. Specifically, for the Sn–O and Si–O bonds, their binding energies increased as x increased from 0.025 to 0.075, reaching the maximum value at x = 0.075. These XPS results clearly demonstrate that the substitution of Ge^{4+} for Sn^{4+} within a certain content range can indeed enhance the covalency of Sn–O and Si–O bonds. Furthermore, the effect of structural stability on dielectric loss was evaluated by the lattice energy (U). The calculation of U can be found in the Supporting Information. As shown in Table S3 in the ESM and Fig. 7(c), Si–O and Sn–O bonds contributed approximately 62% and 22% to the total lattice energy (U_{total}) of $Ca_3Sn_{1-x}Ge_xSi_2O_9$ single-phase ceramics, respectively, indicating their dominant role in structural stability. Remarkably, the variation in U_{total} followed a trend similar to that of the $Q\times f$ values, with the maximum U_{total} (Table S3 in the ESM) and $Q\times f$ values both occurring at x = 0.05. These results demonstrate that for single-phase $Ca_3Sn_{1-x}Ge_xSi_2O_9$ ($0.025 \le x \le 0.125$) ceramics, the enhanced $\overline{r_c}$ (Si–O) and r_c (Sn–O) led to both higher U_{total} and improved $Q\times f$ values. In contrast, for multiphase compositions ($0.15 \le x \le 0.20$), the presence of the low-$Q\times f$ $CaSiO_3$ second phase degraded the microwave dielectric properties, with the deterioration proportional to the $CaSiO_3$ content.

Far-IR serves as an effective tool for investigating intrinsic dielectric loss in microwave dielectric ceramics. The far-IR spectra of single-phase $Ca_3Sn_{1-x}Ge_xSi_2O_9$ ($0.025 \le x \le 0.125$) ceramics were fitted using the Lorenz oscillator model (Eq. (1)) and Fresnel Eq. (2) [61,62].

$$\varepsilon^*(\omega) = \varepsilon_\infty + \sum_{j=1}^{n} \frac{\omega_{pj}^2}{\omega_{oj}^2 - \omega^2 - j\gamma_j\omega} = \varepsilon'(\omega) + i\varepsilon''(\omega) \quad (1)$$

$$R(\omega) = \left| \frac{1 - \sqrt{\varepsilon^*(\omega)}}{1 + \sqrt{\varepsilon^*(\omega)}} \right|^2 \quad (2)$$

The relevant parameters of the above formulas are described in our previous works [31]. As shown in Fig. 7(d), excellent agreement was observed between the fitted spectra (red lines) and experimental data (purple circles). The measured ε_r and dielectric loss are also plotted (five-pointed star circle) for comparison with the fitted values. The fitted ε_r values derived from far-IR spectra were slightly lower than the measured $\varepsilon_{r\text{-}exp}$ values at microwave frequencies, possibly due to extrinsic contributions from defect phonon scattering [63]. Notably, the fitted $Q\times f_{fitted}$ values (Fig. 7(b)) for single-phase $Ca_3Sn_{1-x}Ge_xSi_2O_9$ ($0.025 \le x \le 0.125$) ceramics significantly exceeded the $Q\times f$ values measured at microwave frequencies, demonstrating that Ge^{4+} substitution for Sn^{4+} effectively improved the crystal structure and achieved ultralow intrinsic dielectric loss. The substantial discrepancy between fitted and measured $Q\times f$ values suggests that extrinsic losses, primarily from grain boundary effects (Fig. 6), currently limit the performance of $Ca_3Sn_{1-x}Ge_xSi_2O_9$ ceramics. This indicates that further optimization of the synthesis process could enhance the $Q\times f$ values.

Figures 8(b)–8(e) present the temperature-dependent ε_r of $Ca_3Sn_{1-x}Ge_xSi_2O_9$ ($0.025 \le x \le 0.10$) ceramics measured at 100 kHz, 500 kHz, and 1 MHz. The ε_r values obtained from microwave dielectric measurements showed good agreement with the 1 MHz data. Notably, no distinct ε_r peaks were observed across the temperature range of 25–450 °C, suggesting that Ge^{4+} substitution did not induce significant lattice distortion in $Ca_3Sn_{1-x}Ge_xSi_2O_9$ ceramics. The minor crystal structural perturbations caused by ionic substitution were insufficient to generate prominent ε_r peaks in the ε_r–T curves. This absence of dielectric anomalies (ε_r peaks) further implies the potential for achieving high $Q\times f$ values, as excessive crystal distortion can lead to high dielectric loss. The inset of Figs. 8(b)–8(e) provides the fitted temperature coefficient of ε_r, which initially decreased and then increased with increasing x, following a trend similar to τ_f values (Fig. 8(a)). As illustrated in Fig. 8(a), Ge^{4+} substitution effectively tuned the negative τ_f values to −24.8 ppm/°C in $Ca_3Sn_{1-x}Ge_xSi_2O_9$ ceramics, with this improvement being closely linked to crystal structural evolution.

As summarized in Fig. 8(f) and Table S4 in the ESM, the substitution of small Ge^{4+} for large Sn^{4+} in $Ca_3Sn_{1-x}Ge_xSi_2O_9$ ($0.025 \le x \le 0.075$) ceramics intensified the SnO_6 δ and expanded σ, a consequence of slight structural destabilization induced by small ionic substitution. At higher substitution levels ($0.10 \le x \le 0.125$), Ge^{4+} progressively replaced Si^{4+}, leading to reduced δ and σ, consistent with our previous findings [42]. The increased δ and σ enhanced the restoring forces between ions in the framework of $Ca_3Sn_{1-x}Ge_xSi_2O_9$ ceramics, thereby improving the thermal stability of polarization. The τ_f values followed a trend similar to that of δ and σ. Additionally, the high $V_{Sn/Ge}$ indicated structural stability, correlating with near-zero τ_f values. Thus, the τ_f values of $Ca_3Sn_{1-x}Ge_xSi_2O_9$ ceramics are governed by δ and σ. Remarkably, as shown in Fig. 8(g), optimizing Ge^{4+} substitution for Sn^{4+} in $Ca_3Sn_{1-x}Ge_xSi_2O_9$ ceramics yielded a record-high $Q\times f$ value (120, 413 GHz) and a near-zero τ_f value (−25.8 ppm/°C) among $Ca_3MSi_2O_9$-based ceramics [41,42,64], demonstrating the efficacy of this cooperative optimization strategy for simultaneously enhancing $Q\times f$ and τ_f values in $Ca_3SnSi_2O_9$-based ceramics.

Since ceramic materials exhibit lower intrinsic loss and higher thermal stability than printed circuit board (PCB) substrates, they are promising candidates for manufacturing microwave devices, especially for guided electromagnetic waves. Figure 9(a) shows the unit cell of our substrate-integrated one-dimensional topological metasurface, consisting of top and bottom silver layers and a middle dielectric substrate. The remaining structural parameters are P_x = 5 mm, P_y = 10 mm, l_1 = 1.2 mm, l_2 = 0.6 mm, and w = 3 mm. The distance b between the air stub (marked by the red rectangle) and the center of the structure is a critical parameter used to control the topological properties of the metasurface. The dielectric substrate is made of $Ca_3Sn_{1-x}Ge_xSi_2O_9$ (x = 0.05) ceramics with a thickness of t = 2 mm and a ε_r of 8.88. Figure 9(b) presents the band dispersion of the metastructure with b = 1.25 mm. In this configuration, the structure (denoted as S1) can be analogous to the Su–Schrieffer–Heeger (SSH) model, with equal intercell and intracell coupling, resulting in degeneracy at the boundary of the BZ $k_x = \pi/P_x$ due to band folding.

To lift the band degeneracy and realize a topological phase transition, we considered tuning the distance b between the cell structural center and the air stub along the x-direction. The band

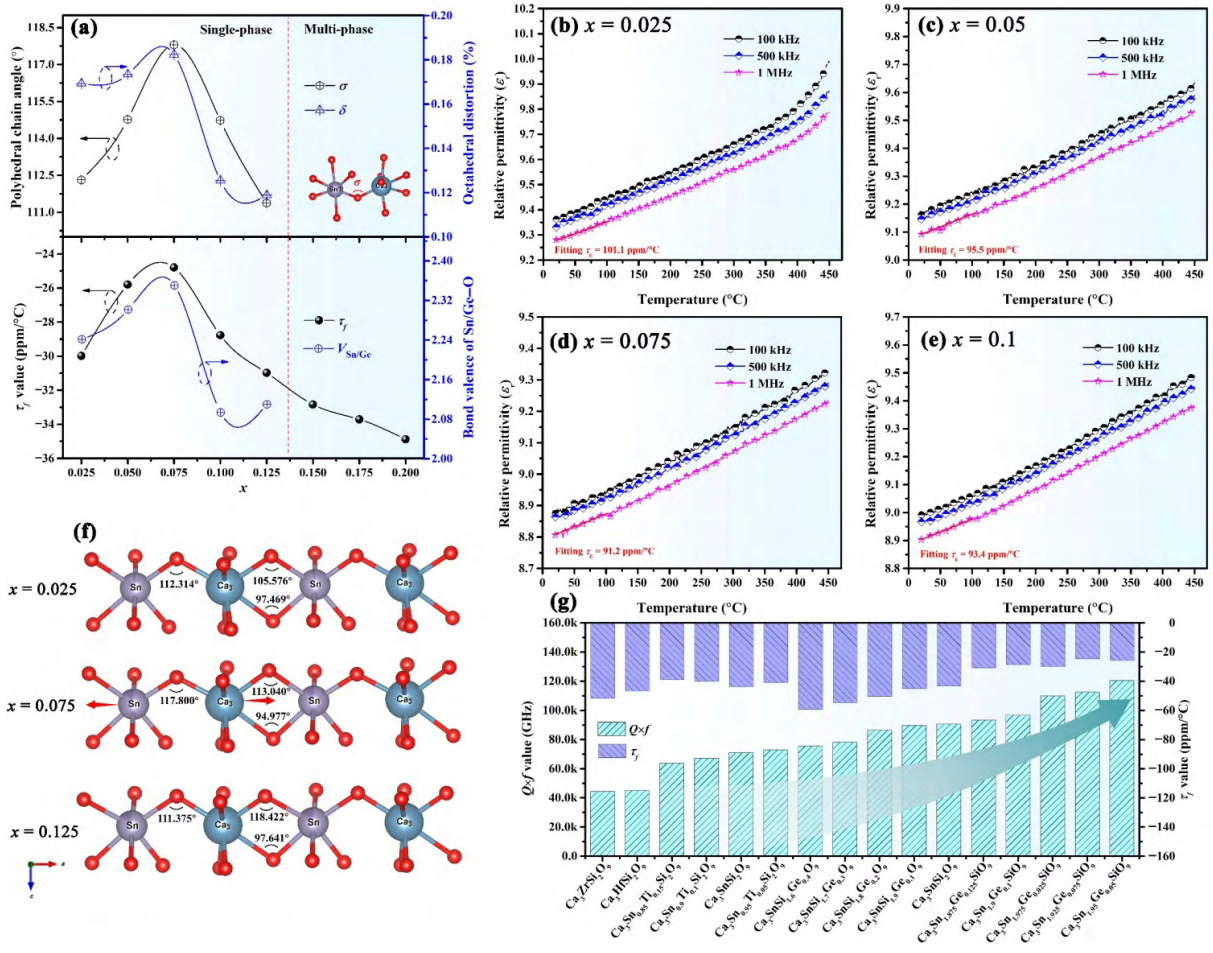

Fig. 8 (a) SnO_6 octahedral distortion, polyhedral chain angle, and bond valence of Si/Ge–O bond, and τ_f values of $Ca_3Sn_{1-x}Ge_xSi_2O_9$ ceramics as a function of x. (b–e) Temperature and frequency dependences of ε_r for $Ca_3Sn_{1-x}Ge_xSi_2O_9$ ceramics. (f) Evolution of polyhedral chains as a function of x. (g) $Q\times f$ and τ_f values of some typical $Ca_3MSi_2O_9$-based ceramics.

structure for b = 1.75 mm (denoted as S2) is shown in Fig. 9(c). A bandgap can be observed between the first and the second bands, spanning from f = 10.36 to 11.43 GHz. For structures with mirror symmetry, the topological property within the bandgap is related to the parities of the eigenstates for the first band at the BZ center and boundary. When the mode parities are identical, the structure is regarded as topologically trivial, and the Zak phase (Z_k) along the periodic direction can be quantized as Z_k = 0. Conversely, when the eigenstates have distinct parity distributions, the structure shows topologically nontrivial properties with $Z_k = \pi$. In most cases, the first band for the photonic crystal at k = 0 is at zero frequency, and the field distribution is even due to the inversion symmetry of the unit cell structure. Therefore, the topological property of the first band can be obtained by analyzing the eigenfield at the boundary of the BZ. The eigenfield at $k_x = \pi/P_x$ for the first band of S2 is shown in the inset of Fig. 9(c). The even field distribution indicates a topologically trivial property. To realize a topologically nontrivial phase, we reduced the distance b between the air stub and the structure center. The band structure for b = 0.75 mm (denoted as S3) is shown in Fig. 9(d). Since S3 can be obtained by shifting S2 by a half period along the x-direction, both structures share essentially the same band structure. However, from a topological perspective, S3 exhibits a topologically nontrivial property within the first E_g, as revealed by the odd distribution of the eigenstate for the first band at $k_x = \pi/P_x$ (shown in the inset of Fig. 9(d)).

Since S2 and S3 exhibit distinct topological properties, a topological interface state (TIS) can be engineered by a junction that combines multiple cells of S2 and S3. We first consider a meta-strip composed of 8 layers of S2 on the left side and 8 layers of S3 on the right side, as shown in the top panel of Fig. 10(a). This meta-strip system supports a quasi-transverse electric and magnetic (TEM) propagation mode, where the electric and magnetic components are oriented vertically and longitudinally within the dielectric substrate around the metallic strip (Fig. S13 in the ESM). Note that the frequency of the TIS can be tuned by the translational deformation Δd (shown in the middle panel of Fig. 10(a)). The bottom panel of Fig. 10(a) and Fig. S14 in the ESM display the fabricated samples, which were obtained by coating silver paste on both sides of the dielectric strip. Figure 10(b) shows the eigenfrequencies of the metasurfaces around the bandgap, where the black and red dots represent the bulk and interface states, respectively. The TIS can be tuned to any frequency within the bandgap by introducing different translational deformations. The corresponding electric field distributions of the TIS are shown in Fig. 10(c), where the field is well confined at the interface and rapidly decays into the bulk regions on either side.

To examine the transmission behavior of the metasurface, we calculate the transmission spectra around the bandgap, as shown in Fig. 10(d). A high transmission line appears within the bandgap, where only the frequency corresponding to the TIS can pass through the metasurface. Specifically, Fig. 10(e) provides detailed views of the transmission from the metasurface with

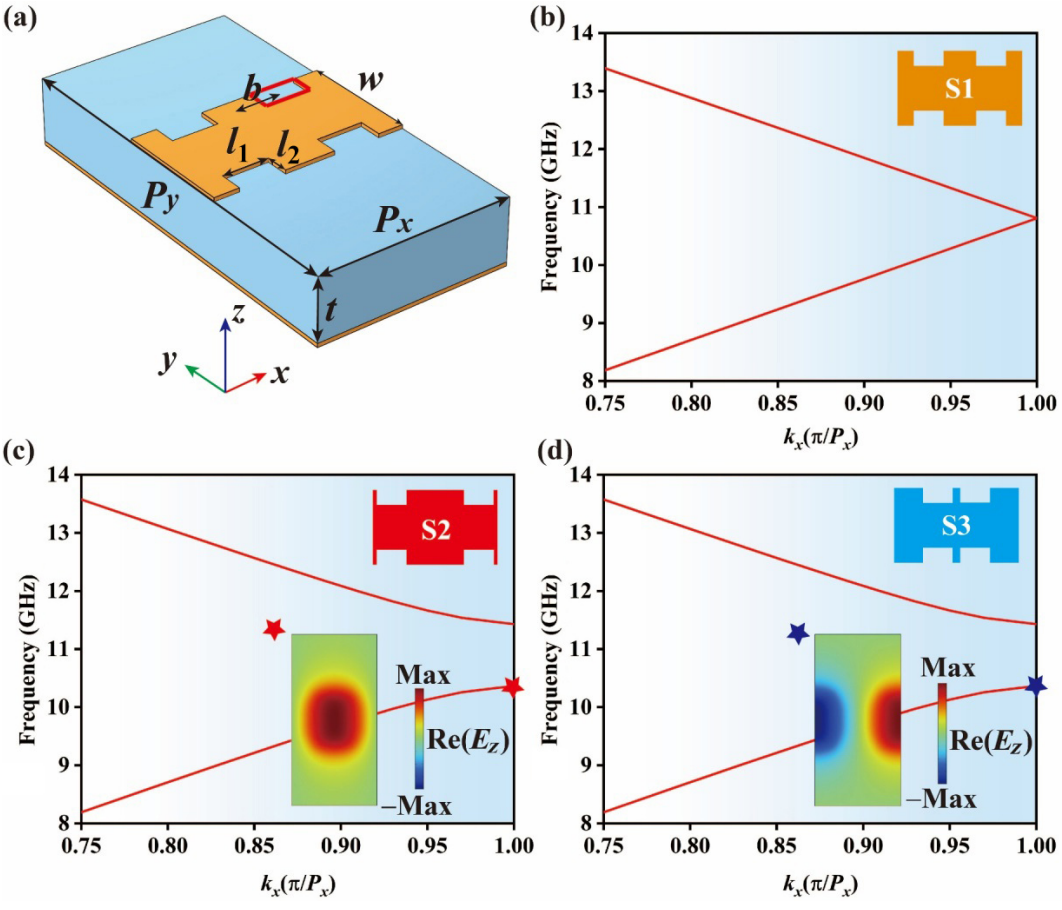

Fig. 9 (a) Schematic of topological metasurface, consisting of two metallic layers on top and bottom sides of dielectric substrate. (b–d) Band structure of the metastructure with (b) b = 1.25 mm, (c) b = 1.75 mm, and (d) b = 0.75 mm. Inset images: eigenfield of the first band at $k_x = \pi/P_x$.

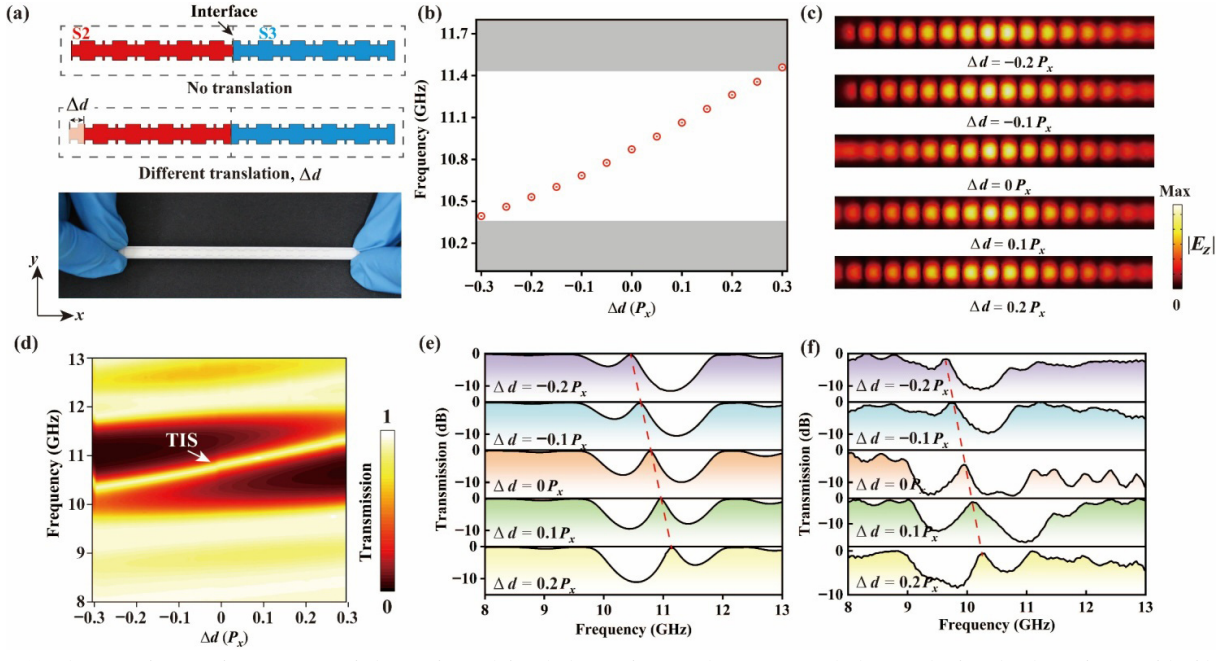

Fig. 10 (a) Schematic of metasurface, consisting of 8 layers of S2 on left and 8 layers of S3 on right. Bottom panel: photograph of overhead view for one of the fabricated samples ($\Delta d = -0.1\ P_x$). (b) Eigenfrequencies of metasurface with different translation deformations. Gray area and red dots represent bulk modes and topological cavity modes, respectively. (c) Electric fields of TIS with $\Delta d = -0.2\ P_x$, $-0.1\ P_x$, 0 P_x, 0.1 P_x, and 0.2 P_x. (d) Transmission spectra of metasurface with difference translation deformations. (e) Simulated transmission spectra of metasurfaces and (f) measured transmission spectra of metasurfaces.

different translational deformations, where the transmission peak shifts toward higher frequencies. Since the band structure of this metasurface is analogous to Bragg scattering between different unit cells, the $Q\times f$ and out-of-band rejection of the filter can be further improved by increasing the number of cells S2 and S3. To verify the simulated results, we measured the transmission spectra

of the fabricated samples using a vector network analyzer, and the result is shown in Fig. 10(f). The measured transmission agrees quite well with the simulation prediction, despite a peak frequency shift, primarily due to fabrication imperfections such as variations in substrate thickness and permittivity, as well as deviations in the parameters of the top metallic strips. In our experiment, the insertion loss is primarily caused by the coupling between the SubMiniature version A (SMA) connectors and the microstrip. However, the pass frequency of the filter can still be effectively identified. The return loss of this metasurface is influenced by the mode transfer between the coupled meta-strip and the TIS. To minimize return loss, it is crucial to precisely design the coupled meta-strip to ensure optimal mode matching. The corresponding S11 spectra of this metasurface with different translation deformations are detailed in Fig. S15 in the ESM. This topological metasurface can be extended to other operating frequencies, even to terahertz with pure dielectric components.

4 Conclusions

This study developed an interpretable machine learning-guided framework that combines accelerated compositional exploration with quantitative mechanistic analysis to identify design strategies for achieving ultrahigh $Q\times f$ values in $Ca_3SnSi_2O_9$-based ceramic systems. Guided by machine learning predictions, the $Ca_3Sn_{1-x}Ge_xSi_2O_9$ system was identified as a promising candidate for obtaining ultrahigh $Q\times f$ values. Accordingly, a series of dense $Ca_3Sn_{1-x}Ge_xSi_2O_9$ ($0.025 \le x \le 0.20$) ceramics was synthesized via solid-phase reaction with systematic investigation of their phase compositions, crystallographic parameters, microstructure, microwave dielectric properties, and topological metasurface filter applications. Within the stoichiometric range of $Ca_3Sn_{1-x}Ge_xSi_2O_9$ ($0.025 \le x \le 0.125$), structural analysis revealed that Ge^{4+} preferentially substituted Sn^{4+}, coordinating with six oxygen atoms to form [Sn/GeO_6] octahedra in single-phase $Ca_3Sn_{1-x}Ge_xSi_2O_9$ ($0.025 \le x \le 0.075$) ceramics. However, in compositions with higher Ge^{4+} content ($0.10 \le x \le 0.125$), steric constraints imposed by the smaller ionic radius of Ge^{4+} relative to Sn^{4+} led to partial substitution of Si^{4+}, resulting in the formation of [Si/GeO_4] tetrahedra rather than additional [Sn/GeO_6] octahedra. ε_r was found to be governed by ionic polarizability and the $CaSiO_3$ second phase. Appropriate Ge^{4+} substitution for Sn^{4+} significantly enhanced the $Q\times f$ values of $Ca_3Sn_{1-x}Ge_xSi_2O_9$ ($0.025 \le x \le 0.075$) ceramics, attributed to the increased r_c of Sn–O and Si–O bonds and elevated U_{total}. Further Ge^{4+} substitution ($x \ge 0.10$) degraded $Q\times f$ values due to reduced r_c of Sn–O and Si–O bonds, decreased U, and the emergence of the $CaSiO_3$ phase. The τ_f values of single-phase $Ca_3Sn_{1-x}Ge_xSi_2O_9$ ($0.025 \le x \le 0.125$) ceramics exhibited a strong dependence on crystal structural distortions. Specifically, the τ_f values of single-phase $Ca_3Sn_{1-x}Ge_xSi_2O_9$ ceramics were predominantly influenced by the local distortions in CaO_7–SnO_6 polyhedral chains (chain angles) and distortion within the [SnO_6] octahedron. Enhanced distortion in both structural features contributed to the achievement of near-zero τ_f values. These insights into the structure–property relationships pave the way for designing high-performance dielectric ceramics. The optimal $Ca_3Sn_{1-x}Ge_xSi_2O_9$ ($x = 0.05$) ceramics exhibit excellent properties ($\varepsilon_r = 8.88$, $Q\times f = 120{,}413$ GHz, and $\tau_f = -25.8$ ppm/°C) and was successfully applied in a tunable topological metasurface filter (9.6–10.3 GHz). In summary, this study's innovations lie in the ML-guided framework, clarified the substitution mechanism, and established structure–property relationships, providing a rational strategy for designing high-performance microwave dielectric ceramics.

Acknowledgements

The authors acknowledge financial support from the National Natural Science Foundation of China (Nos. 52402153 and 12504510), the Natural Science Foundation of Wuhan (No. 2025040601020165), and the Foundation of the Open Research Fund of Anhui Key Laboratory of Low Temperature Co-fired Materials (No. HNLC2025A01). The authors are grateful to the National Synchrotron Radiation Laboratory (NSRL) for the IR measurements.

Availability of data and materials

The data that support the findings of this study are available from the corresponding author upon reasonable request.

Competing interests

The authors have no competing interests to declare that are relevant to the content of this article.

Electronic Supplementary Material

Supplementary material is available in the online version of this article at https://doi.org/10.26599/JAC.2026.9221285.

References

[1] Xie MJ, Lai YM, Xiang PW, *et al.* The entropy effect on the structure and microwave dielectric properties of high-entropy $Li_x(MgZnCoNi)_{(1-x)/4}Al_2O_{4-\delta}$ ceramics. *Chem Eng J* 2024, **496**: 154132.

[2] Wang W, Wang X, Bao J, *et al.* Low-permittivity $BaCuSi_4O_{10}$-based dielectric ceramics: An available solution to connect low temperature cofired ceramic technology and millimeter-wave communications. *Chem Eng J* 2024, **494**: 153172.

[3] Du QB, Ma LZ, Duan JH, *et al.* Crystal structure, sintering behavior, and microwave dielectric properties of LiF-tailored high entropy $Li_2Mg_6ZnTi_6O_{20}$ ceramics. *J Mater Sci Technol* 2025, **220**: 290–298.

[4] Wu FF, Sun RX, Du C, *et al.* P^{5+}-enhanced novel samarium niobate ultralow-loss microwave ceramics as dielectric resonator for X-band antenna applications. *Adv Funct Mater* 2025, **35**: 2421225.

[5] Yang Y, Fang WS, Lin HX, *et al.* $SrGa_{12}O_{19}$: The first low-ε_r Ga-based microwave dielectric ceramic with anomalous positive τ_f. *J Adv Ceram* 2024, **13**: 1432–1441.

[6] Du QB, Jiang LX, Ma LZ, *et al.* Lattice evolution, order transformation, and microwave dielectric properties of the $Zn_{1-x}Li_{2x}TiO_3$ ($0 \le x \le 1$) system ceramics. *J Adv Ceram* 2024, **13**: 1178–1188.

[7] Tian HR, Zhang XH, Zhang ZD, *et al.* Low-permittivity $LiLn(PO_3)_4$ (Ln = La, Sm, Eu) dielectric ceramics for microwave/millimeter-wave communication. *J Adv Ceram* 2024, **13**: 602–620.

[8] Xiao M, Zhang ZQ, Chan CT. Surface impedance and bulk band geometric phases in one-dimensional systems. *Phys Rev X* 2014, **4**: 021017.

[9] Lu CC, Wang CY, Xiao M, *et al.* Topological rainbow concentrator based on synthetic dimension. *Phys Rev Lett* 2021, **126**: 113902.

[10] Zheng JJ, Zhou HY, Li JY, *et al.* Perfect light absorber with a PT phase transition via coupled topological interface states. *Photonics Res* 2023, **11**: 517.

[11] Kruk S, Poddubny A, Smirnova D, *et al.* Nonlinear light generation in topological nanostructures. *Nat Nanotechnol* 2019, **14**: 126–130.

[12] Wei GC, Wang BB, Du K, *et al.* Angle-insensitive transmission and absorption with a PT phase transition *via* coupled interface states in hybrid one-dimensional photonic crystal heterostructures. *Phys Rev A* 2024, **109**: 053504.

[13] Zhang ZD, Yu SY, Xu H, *et al.* Monolithic strong coupling of topological surface acoustic wave resonators on lithium niobate. *Adv Mater* 2024, **36**: 2312861.

[14] Liu MD, Chen HH, Wang ZY, *et al.* On-chip topological photonic crystal nanobeam filters. *Nano Lett* 2024, **24**: 1635–1641.

[15] Fujishima S. The history of ceramic filters. *IEEE T Ultrason Ferr* 2000, **47**: 1–7.
[16] Hill MD, Cruickshank DB, MacFarlane IA. Perspective on ceramic materials for 5G wireless communication systems. *Appl Phys Lett* 2021, **118**: 120501.
[17] Du K, Song XQ, Li J, *et al.* Optimised phase compositions and improved microwave dielectric properties based on calcium tin silicates. *J Eur Ceram Soc* 2019, **39**: 340–345.
[18] Du K, Wen TL, Zhou MD, *et al.* Optimized phase compositions and microwave dielectric properties of low loss $Ca_2Sn_2Al_2O_9$-based ceramics by M^{4+} substitution. *J Am Ceram Soc* 2023, **106**: 2941–2952.
[19] Kamutzki F, Schneider S, Barowski J, *et al.* Silicate dielectric ceramics for millimetre wave applications. *J Eur Ceram Soc* 2021, **41**: 3879–3894.
[20] Ni LZ, Li LX, Du MK, *et al.* Wide temperature stable $Ba(Mg_xTa_{2/3})O_3$ microwave dielectric ceramics with ultra-high-Q applied for 5G dielectric filter. *Ceram Int* 2021, **47**: 1034–1039.
[21] Liu B, Hu CC, Huang YH, *et al.* Crystal structure, infrared reflectivity spectra and microwave dielectric properties of $CaAl_2O_4$ ceramics with low permittivity. *J Alloys Compd* 2019, **791**: 1033–1037.
[22] Zhou MK, Chen HT, Zhou GH, *et al.* Co-effects of Nb_2O_5 and stoichiometric deviations on the microwave dielectric properties of $Y_3Al_5O_{12}$. *Ceram Int* 2022, **48**: 18651–18657.
[23] Huang CL, Wang JJ, Huang CY. Sintering behavior and microwave dielectric properties of nano alpha-alumina. *Mater Lett* 2005, **59**: 3746–3749.
[24] Zhou HF, Lu CM, Li SX, *et al.* Phase composition, sintering behavior and mirowave dielectric properties of novel high Q $Ca_3Al_2(GeO_4)_3$ ceramic. *Mater Lett* 2020, **263**: 127240.
[25] Du K, Yin CZ, Zhu W, *et al.* Phase compositions and crystal structure of Sn-deficient $Ca_2Sn_2Al_2O_9$ microwave dielectric ceramics with high $Q\times f$ values. *Ceram Int* 2023, **49**: 202–209.
[26] Luo YL, Liu XT, Zeng ZH, *et al.* Optimised phase compositions and achieved ultra-high $Q\times f$ values in $Ca_{(2+y)}Sn_2Al_{(2+x)}O_{(9+1.5x+y)}$ ceramics by composition modulation. *Mater Chem Phys* 2024, **328**: 129982.
[27] Sugiyama T, Tsunooka T, Kakimoto KI, *et al.* Microwave dielectric properties of forsterite-based solid solutions. *J Eur Ceram Soc* 2006, **26**: 2097–2100.
[28] Fang J, Mao MM, She YX, *et al.* Phase stabilization strategy for robust high $Q\times f$ values in $MgSiO_3$-based ceramics for millimeter-wave applications. *J Eur Ceram Soc* 2025, **45**: 117586.
[29] Joseph T, Sebastian MT, Jantunen H, *et al.* Tape casting and dielectric properties of $Sr_2ZnSi_2O_7$-based ceramic–glass composite for low-temperature co-fired ceramics applications. *Int J Appl Ceram Tec* 2011, **8**: 854–864.
[30] Liu ZY, Du K, Li CY, *et al.* Design and fabrication of a C-band patch antenna with low loss $BaM_4Si_5O_{17}$ microwave dielectric ceramics. *ACS Appl Mater Inter* 2024, **16**: 57325–57333.
[31] Du K, Liu ZY, Wen TL, *et al.* Crystal structural dependence of microwave dielectric characteristics of novel $BaM_2N_3O_{10}$ trisilicate ceramics. *J Alloys Compd* 2024, **1002**: 175377.
[32] Viegas JI, Moreira RL, Dias A. Optical-vibration and intrinsic dielectric properties of low-k high-Q Zn_2GeO_4 ceramics. *J Phys Chem Solids* 2021, **148**: 109693.
[33] Du K, Yin CZ, Zhu W, *et al.* An evaluation of the impact of crystal structure on microwave dielectric properties of novel titanite-type $CaMGeO_5$ ceramics. *J Eur Ceram Soc* 2022, **42**: 7448–7454.
[34] Tang Y, Zhang ZW, Li J, *et al.* $A_3Y_2Ge_3O_{12}$ (A = Ca, Mg): Two novel microwave dielectric ceramics with contrasting τ_f and $Q\times f$. *J Eur Ceram Soc* 2020, **40**: 3989–3995.
[35] Xiang HC, Li CC, Jantunen H, *et al.* Ultralow loss $CaMgGeO_4$ microwave dielectric ceramic and its chemical compatibility with silver electrodes for low-temperature cofired ceramic applications. *ACS Sustain Chem Eng* 2018, **6**: 6458–6466.
[36] Li J, Tang Y, Zhang ZW, *et al.* Two novel garnet $Sr_3B_2Ge_3O_{12}$ (B = Yb, Ho) microwave dielectric ceramics with low permittivity and high Q. *J Eur Ceram Soc* 2021, **41**: 1317–1323.
[37] He YH, Yang QL, Wei XL, *et al.* $AY_2Al_4GeO_{12}$ (A = Ca, Mg) ceramics: Phase composition, microstructure, lattice vibration, bond characteristics, and microwave dielectric properties. *Ceram Int* 2024, **50**: 12310–12318.
[38] Chen CX, Wu SP, Fan YX. Synthesis and microwave dielectric properties of B_2O_3-doped Mg_2GeO_4 ceramics. *J Alloys Compd* 2013, **578**: 153–156.
[39] Jiang C, Wu SP, Ma Q, *et al.* Synthesis and microwave dielectric properties of Nd_2SiO_5 ceramics. *J Alloys Compd* 2012, **544**: 141–144.
[40] Du K, Yin CZ, Guo YB, *et al.* Phase transition, infrared spectra, and microwave dielectric properties of temperature-stable $CaSnSi_{1-x}Ge_xO_5$ ceramics. *Ceram Int* 2021, **47**: 24781–24792.
[41] Song XQ, Du K, Zhang XZ, *et al.* Crystal structure, phase composition and microwave dielectric properties of $Ca_3MSi_2O_9$ ceramics. *J Alloys Compd* 2018, **750**: 996–1002.
[42] Du K, Yin CZ, Guo YB, *et al.* The relationship between crystal structure and modified microwave dielectric properties of $Ca_3SnSi_{2-x}Ge_xO_9$ ceramics. *J Am Ceram Soc* 2022, **105**: 1253–1264.
[43] Ramarao SD, Murthy VRK. Crystal structure refinement and microwave dielectric properties of new low dielectric loss $AZrNb_2O_8$ (A: Mn, Zn, Mg and Co) ceramics. *Scripta Mater* 2013, **69**: 274–277.
[44] Butler KT, Davies DW, Cartwright H, *et al.* Machine learning for molecular and materials science. *Nature* 2018, **559**: 547–555.
[45] Qin JC, Liu ZF, Ma MS, *et al.* Structure and microwave dielectric properties of gillespite-type $ACuSi_4O_{10}$ (A = Ca, Sr, Ba) ceramics and quantitative prediction of the $Q\times f$ value via machine learning. *ACS Appl Mater Inter* 2021, **13**: 17817–17826.
[46] Shannon RD. Revised effective ionic radii and systematic studies of interatomic distances in halides and chalcogenides. *Acta Crystallogr A* 1976, **32**: 751–767.
[47] Yang HY, Gao C, Jiang DH, *et al.* Machine learning assisted prediction for the coefficient of thermal expansion of binary crystals. *J Adv Ceram* 2025, **14**: 9221117.
[48] Wei C, Cui ZJ, Li HK, *et al.* An interpretable machine learning model for Mn-based cathode development: Mapping synthesis parameters to cycling stability. *J Mater Chem A* 2025, **13**: 31264–31278.
[49] Hakki BW, Coleman PD. A dielectric resonator method of measuring inductive capacities in the millimeter range. *IEEE T Microw Theory* 1960, **8**: 402–410.
[50] Kresse G, Furthmüller J. Efficient iterative schemes for *ab initio* total-energy calculations using a plane-wave basis set. *Phys Rev B* 1996, **54**: 11169–11186.
[51] Kresse G, Hafner J. *Ab initio* molecular dynamics for liquid metals. *Phys Rev B* 1993, **47**: 558–561.
[52] Perdew J, Burke K, Ernzerhof M. Generalized gradient approximation made simple. *Phys Rev Lett* 1996, **77**: 3865–3868.
[53] Hammer B, Hansen LB, Nørskov JK. Improved adsorption energetics within density-functional theory using revised Perdew–Burke–Ernzerhof functionals. *Phys Rev B* 1999, **59**: 7413–7421.
[54] Lu T, Chen FW. Meaning and functional form of the electron localization function. *Acta Phys Sin-Ch Ed* 2011, **27**: 2786–2792.
[55] Lu T, Chen FW. Multiwfn: A multifunctional wavefunction analyzer. *J Comput Chem* 2012, **33**: 580–592.
[56] Lu T. A comprehensive electron wavefunction analysis toolbox for chemists, Multiwfn. *J Chem Phys* 2024, **161**: 082503.
[57] Shi MG, Ma SY, Xia WS, *et al.* Effects of oxygen vacancy on bond ionicity, lattice energy, and microwave dielectric properties of CeO_2 ceramics with Yb^{3+} substitution. *J Adv Ceram* 2024, **13**: 247–254.
[58] Liu K, Zhang DN, Lei YD, *et al.* Mechanisms affecting microwave dielectric properties of $Li_2Mg_2TiO_5$ ceramics based on lithium excess. *J Alloys Compd* 2024, **1008**: 176717.

[59] Wang H, He QF, Gao X, *et al.* Multifunctional high entropy alloys enabled by severe lattice distortion. *Adv Mater* 2024, **36**: 2305453.
[60] Li CY, Du K, Zhou MD, *et al.* Achieving ultralow thermal expansion and excellent microwave dielectric properties in osumilite-type $BaMg_2Al_6Si_{9-x}Ge_xO_{30}$ ceramics. *J Adv Ceram* 2025, **14**: 9221146.
[61] Wu FF, Zhou D, Du C, *et al.* Design and fabrication of a satellite communication dielectric resonator antenna with novel low loss and temperature-stabilized $(Sm_{1-x}Ca_x)(Nb_{1-x}Mo_x)O_4$ (x = 0.15–0.7) microwave ceramics. *Chem Mater* 2023, **35**: 104–115.
[62] Wu FF, Zhou D, Du C, *et al.* Design of a sub-6 GHz dielectric resonator antenna with novel temperature-stabilized $(Sm_{1-x}Bi_x)NbO_4$ (x = 0–0.15) microwave dielectric ceramics. *ACS Appl Mater Inter* 2022, **14**: 7030–7038.
[63] Liu B, Li L, Liu XQ, *et al.* Structural evolution of $SrLaAl_{1-x}(Zn_{0.5}Ti_{0.5})_xO_4$ ceramics and effects on their microwave dielectric properties. *J Mater Chem C* 2016, **4**: 4684–4691.
[64] Kan A, Ogawa H, Ohsato H. Synthesis and crystal structure–microwave dielectric property relations in Sn-substituted $Ca_3(Zr_{1-x}Sn_x)Si_2O_9$ solid solutions with cuspidine structure. *Jpn J Appl Phys* 2007, **46**: 7108.